SIAM J. IMAGING SCIENCES
Vol. 2, No. 4, pp. 1003–1030

Imaging by Modification: Numerical Reconstruction of Local Conductivities from Corresponding Power Density Measurements*

Y. Capdeboscq†, J. Fehrenbach‡, F. de Gournay§, and O. Kavian§

Abstract. We discuss the reconstruction of the impedance from the local power density. This study is motivated by a new imaging principle which allows us to recover interior measurements of the energy density by a noninvasive method. We discuss the theoretical feasibility in two dimensions, and propose numerical algorithms to recover the conductivity in two and three dimensions. The efficiency of this approach is documented by several numerical simulations.

Key words. inverse problem, conductivity, imaging

AMS subject classifications. 35R30, 74B05, 92C55

DOI. 10.1137/080723521

1. Introduction.

Let Ω be a simply connected open set in $\mathbb{R}^d$, $d = 2$ or 3, with a C^1 boundary $\partial\Omega$. Given an integer $N \geq 1$, let $(g_i)_{1\leq i\leq N}$ be N continuous functions in $H^{1/2}(\partial\Omega)$, and given $\sigma \in L^\infty(\Omega)$, consider u_i, the solution to the conductivity problems

$$\operatorname{div}(\mathrm{e}^\sigma \nabla u_i) = 0 \text{ in } \Omega, \quad u_i = g_i \text{ on } \partial\Omega \quad \forall\, i \in \{1,\dots,N\}, \tag{1.1}$$

and define $(S_{ij})_{1\leq i,j\leq N} \in L^1(\Omega)$ by

$$S_{ij} := \mathrm{e}^\sigma \nabla u_i \cdot \nabla u_j \text{ a.e. in } \Omega. \tag{1.2}$$

This work is devoted to the theoretical and numerical study of the following inverse problem: given the functions $(S_{ij})_{1\leq i,j\leq N}$ on $\omega \subset\subset \Omega$, and given σ near the boundary of the domain, recover σ inside ω.

This question is motivated by a new imaging method for the determination of the conductivity inside the domain Ω, which relies on both electrical impedance tomography and ultrasonic wave focusing. A focused ultrasonic wave slightly modifies the conductivity within the domain, which in turn allows one to recover the energy densities S_{ij}. This method is described in the recent work of Ammari et al. [2]. In this paper, a first inversion algorithm is proposed for recovering e^σ from S_{11}, S_{22}, and S_{12}. It recovers data very successfully.

Yet, many questions are left unanswered. In [2], the case of a full energy density map is considered, i.e., $\omega = \Omega$, and the ad hoc algorithm proposed cannot be extrapolated simply

*Received by the editors May 8, 2008; accepted for publication (in revised form) June 4, 2009; published electronically October 14, 2009. This paper is the result of a collaboration while all of the authors were at the LMV (Laboratoire de Mathématiques de Versailles). This was made possible by ANR project EchoScan (AN-06-Blan-0089).

http://www.siam.org/journals/siims/2-4/72352.html

†Mathematical Institute, University of Oxford, Oxford OX1 3LB, UK (yves.capdeboscq@maths.ox.ac.uk).

‡IMT, Université Paul Sabatier, CNRS, 31062 Toulouse, France (fehren@mip.ups-tlse.fr).

§LMV, Université Versailles-Saint Quentin, CNRS, 78035 Versailles, France (frederic.de.gournay@uvsq.fr, otared.kavian@uvsq.fr).

when imaging smaller subdomains. This algorithm relies in a fundamental way on the existence of several measurements (at least two) and diverges in general for one measurement. Furthermore, because it is based on a perturbation approach, its stability cannot be guaranteed a priori.

This problem is studied here from a different perspective, that of optimal control. Consider the case of one current, that is, one data S_{11}. It is clear that the inversion can be reformulated as a minimization problem, such as the following:

$$\text{Minimize } \mathcal{J}(\sigma) := \int_\omega j\left(E(\sigma), x\right)\, dx \text{ over all } \sigma \in L^\infty(\Omega), \tag{1.3}$$

where $j : \mathbb{R} \times \Omega \longrightarrow [0, \infty)$ is an appropriately chosen sufficiently smooth function and $j(s, x) = 0$ if and only if $s = S_{11}(x)$, and

$$E(\sigma) := \mathrm{e}^\sigma |\nabla u|^2 \text{ with } \operatorname{div}\left(\mathrm{e}^\sigma \nabla u\right) = 0 \text{ in } \Omega, \quad u = g_1 \text{ on } \partial\Omega. \tag{1.4}$$

The solving methods and numerical results presented in this paper follow this formulation, or its multidata counterpart. To assess the quality of the inversion procedure, it is necessary to establish what can be recovered. Note that, even though the problem under consideration is related to electrical impedance tomography, we cannot rely on the theoretical results obtained for that problem: indeed we cannot assume that the Steklov–Poincaré operator, or the Dirichlet-to-Neumann map, is known, since only a limited number of voltage potentials $(g_i)_{1\le i\le N}$ are imposed on the boundary.

In fact, the nature of the inversion is quite different. For instance, in the one-dimensional case in which $\Omega = (0, 1)$, with one data S_{11} known everywhere on $(0, 1)$, the conductivity is easily determined. Indeed, for some constant C we have $\mathrm{e}^\sigma u_x = C$ and thus $S_{11} = \mathrm{e}^{-\sigma} C^2$. Also assuming, for instance, $g_1(1) - g_1(0) = 1$, one infers that $C \int_0^1 \mathrm{e}^{\sigma(x)} dx = u(1) - u(0) = 1$ and $C = \int_0^1 S_{11}(x) dx$ so that C is determined by S_{11} and finally σ is completely determined. In contrast, using electrical impedance tomography, only the average of the conductivity over $(0, 1)$ can be recovered.

Of paramount importance for this complete reconstruction is the knowledge of S_{11} everywhere on $(0, 1)$. In any dimension, if the data is known only on a subdomain ω strictly included in Ω, one can hope to recover only the log-conductivity σ up to an additive constant, as illustrated by the following example. Suppose for simplicity that $d = 2$, that the domain is a disk of radius 1 centered at the origin, and that the log-conductivity is radial, given by

$$\sigma := \begin{cases} \log \gamma_0 & \text{if } r < \frac{1}{2}, \\ \log \gamma_1 & \text{if } \frac{1}{2} < r < \frac{1}{\sqrt{2}}, \\ 0 & \text{if } \frac{1}{\sqrt{2}} < r < 1. \end{cases}$$

In such a case, for a boundary condition of the form $g = c_1 \cos(\theta) + s_1 \sin(\theta)$, $\theta \in (0, 2\pi)$, the solution u, and, in turn, the data, can be computed explicitly by separation of variables. The solution u is given in polar coordinates by $u(r, \theta) = p_1 \left(c_1 \cos(\theta) + s_1 \sin(\theta)\right) r$ for $r \le 1/2$, where the constant p_1 is given by

$$p_1 = \frac{16\gamma_1}{\gamma_1^2 + 9\gamma_1 + 3\gamma_1\gamma_0 + 3\gamma_0}.$$

We therefore see that selecting γ_0 and γ_1 such that $\gamma_0 = \gamma_1(7-\gamma_1)/3(1+\gamma_1)$ will yield the same data as that of a homogeneous medium of log-conductivity $\sigma = 0$. Counterexamples for polynomial boundary conditions $g = \sum_{k=1}^{N} c_k \cos(k\theta) + s_k \sin(k\theta)$ can be constructed similarly by introducing N annuli of different conductivities between the disk of radius $1/2$ and the exterior boundary.

In section 2, we investigate the theoretical reconstruction of the log-conductivity. First we show that if $s_1 = \mathrm{e}^{\sigma/2}\nabla u_1$ is known, that is, if not only the modulus $S_{11}^{1/2}$ but also the direction $\theta_1 := |\nabla u_1|^{-1}\nabla u_1$ of the gradient ∇u_1 is known, then the conductivity may be determined up to a multiplicative constant, under some regularity assumption (this means that the *log-conductivity* σ is determined up to an additive constant). Then, we show that if two *diffeomorphic measurements* s_1 and s_2 are performed, yielding a set of three data S_{11}, S_{22}, and S_{12}, the direction θ_1 can also be recovered up to a constant angle. Note that when $\omega = \Omega$, using the fact that σ is known in a neighborhood of $\partial\Omega$, both constants involved in the determination of the log-conductivity and that of the direction θ_1 can be recovered. By *diffeomorphic measurements* we mean that the solutions u_1, u_2 satisfy

$$\det(\nabla u_1, \nabla u_2) > 0 \quad \text{or, equivalently,} \quad \det(s_1, s_2) > 0 \text{ a.e. in } \omega. \tag{1.5}$$

The difficulty is that we want to ensure that we have performed diffeomorphic measurements by a judicious choice of g_1 and g_2, independently of σ. The following theorem of Alessandrini and Nesi [1], extending the classical theorems of Radó (1926), Kneser (1926), and Choquet (1945) for harmonic maps, shows that in two dimensions, there are many such possible choices. We formulate the theorem for the scalar case, although in [1] the result is shown for matrix-valued conductivities.

Theorem 1.1 (Alessandrini and Nesi [1]). *Let $\Omega \subset \mathbb{R}^2$ be a bounded simply connected open set, whose boundary $\partial\Omega$ is a simple closed curve. Let $\mathbf{g} = (g_1, g_2)$ be a mapping $\partial\Omega \to \mathbb{R}^2$ which is a homeomorphism of $\partial\Omega$ onto a convex closed curve $\mathcal{C}$, and let D denote the bounded convex domain bounded by $\mathcal{C}$. Let $\sigma \in L^\infty(\Omega)$, and let $U = (u_1, u_2)$ be the e^σ-harmonic mapping whose components u_1, u_2 are solutions of the Dirichlet problems*

$$\begin{aligned} \operatorname{div}(\mathrm{e}^\sigma \nabla u_i) &= 0 \ \text{in } \Omega, \\ u_i &= g_i \ \text{on } \partial\Omega, \end{aligned}$$

with $g_i \in H^1(\Omega) \cap C(\overline{\Omega})$ and $i = 1, 2$. Then U is a homeomorphism of $\overline{\Omega}$ onto $\overline{D}$. In particular we have either

$$\forall\, \omega \subset\subset \Omega,\ \det(\nabla u_1, \nabla u_2) > 0 \ \text{ a.e. in } \omega$$

or

$$\forall\, \omega \subset\subset \Omega,\ \det(\nabla u_1, \nabla u_2) < 0 \ \text{ a.e. in } \omega.$$

As a consequence, assuming that Ω is convex and sufficiently smooth, taking measurements with, say, $g_1 = x_1$ and $g_2 = x_2$ (that is, $\mathbf{g} = Id$), we are guaranteed that condition (1.5) holds.

Unfortunately, such a result is not true when $d = 3$, even in the harmonic case as was proved by Laugesen [9], and changes of signs in the determinant can happen at arbitrarily small scales; see Briane, Milton, and Nesi [4]. Geometries such as the one sketched in Figure 1

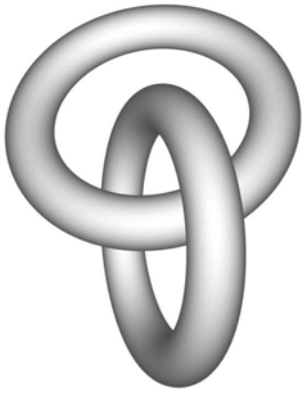

Figure 1. *A problematic configuration for the conductivity when $d = 3$ and when the conductivity is very high in the annuli compared to that of the background medium.*

provide counterexamples. These results indicate that an extension of our approach to the uniqueness problem to the three-dimensional case is likely to fail.

In section 3, we adopt an optimization point of view and consider the inverse problem as described in (1.3). More precisely, we introduce two functionals

$$\mathcal{J}_1(\sigma) := \int_\omega \left(\mathrm{e}^{\sigma/2} \, |\nabla u| - S_{11}^{1/2} \right)^2$$

and

$$\mathcal{J}_2(\sigma) := \frac{1}{2} \sum_{i=0}^{n} \left(\int_{\omega_i} \mathrm{e}^{\sigma} \, |\nabla u|^2 \, dx - \int_{\omega_i} S_{11} \, dx \right)^2,$$

where $(\omega_i)_{1 \le i \le n}$ is a partition of ω. We compute their differentials and show that strict convexity of such functionals cannot be guaranteed a priori. This fact is not related to the particular choice of integrand (cost functions j in the language of optimal control (1.3)). We then discuss how a weaker lower bound on the Hessian can be used to improve minimization procedures, and why several electric measurements are beneficial.

For the sake of concision, the gradient descent method used to minimize $\mathcal{J}_1$ is not detailed. In section 4, we detail the implementation of the Gauss–Newton method used to minimize $\mathcal{J}_2$. For an increased numerical efficiency, the Jacobian matrix of the cost function is evaluated differently on fine and coarse meshes. This leads to a nested grid algorithm, that is, where nested subgrids appear. For three-dimensional computations, the involved number of degrees of freedom prohibits the resolution of very fine scale problems. We believe that our algorithm allows us to circumvent this difficulty if a fine resolution is needed only in a small area of the domain.

Finally in sections 5 and 6, numerical examples are presented and discussed. We first consider the two-dimensional case. First we verify that perfect convergence is achieved in the most favorable case, that is, when the data and the reconstruction are done on the same mesh. We then turn to the question of stability and perform the reconstruction on an arbitrary uniform mesh, unrelated to the one used to create the data, and introduce noise. We

see that the algorithm still converges very convincingly and reacts to the noise in a stable manner. Finally, we test a patchwork approach, that is, a simultaneous resolution on different overlapping subdomains. We then turn to the three-dimensional case. The numerical issues of interpolation between different meshes are not addressed in this work, but we consider the case of noisy data. In that case the nested grids resolution method is illustrated on a half-sphere—a domain resembling a breast, since breast cancer detection is an application we have in mind.

2. On the theoretical reconstruction of the conductivity in two dimensions. In this section we show that, possibly up to two constant parameters, the conductivity can be determined from two diffeomorphic measurements. In fact, we could exhibit an explicit inversion formula from Propositions 2.1 and 2.2, using formulae (2.4) and (2.13), which would simplify the inversion to the evaluation of two real parameters, easily found from the near boundary information available for σ. We chose not to do so for two reasons. First, these formulae are exclusively two-dimensional, as they rely in an essential way on the fact that divergence-free fields are curls, and Theorem 1.1 is used frequently. Finally, both (2.4) and (2.13) require us to differentiate the measured data, and this is a well-known source for instability.

Proposition 2.1. *Assume that $d = 2$ and $\sigma \in W^{1,p}(\Omega)$ for some $p > 2$ and that Ω is a smooth bounded domain. Let u_1 be the solution of (1.1) for $i = 1$. Assume that $S_{11} \neq 0$ in Ω and furthermore that $s_1 := \mathrm{e}^{\sigma/2}\nabla u_1$ is known almost everywhere in $\omega \subset \Omega$, and that*

$$|\nabla u_1|^{-1} \in L^2(\Omega) \quad \text{and} \quad |\nabla u_1|^{-2}\partial_{ij}u_1 \in L^2(\Omega). \tag{2.1}$$

Then σ is known in ω up to an additive constant. Without further assumptions, the additive constant cannot always be determined.

Proof. Let $\varphi \in H_0^1(\Omega)$ be a test function. Testing (1.1) against φ we obtain

$$\int_\Omega \mathrm{e}^{\sigma/2} s_1 \cdot \nabla\varphi \, dx = 0.$$

Recall the Sobolev embeddings $H_0^1(\Omega) \subset L^q(\Omega)$ for all $q < \infty$ and that $W^{1,p}(\Omega) \subset C(\overline{\Omega})$ for $p > 2$. Now if $\varphi \in H_0^1(\Omega)$, since $\nabla\sigma \in L^p(\Omega)$, upon choosing q appropriately one checks that $(\nabla\sigma \cdot s_1)\varphi \in L^1(\Omega)$. This means that for any $\varphi \in H_0^1(\Omega)$ we have $\mathrm{e}^{\pm\sigma/2}\varphi \in H_0^1(\Omega)$, and therefore in the above identity we may replace φ by $\mathrm{e}^{-\sigma/2}\varphi$, which yields, for all $\varphi \in H_0^1(\Omega)$,

$$\int_\Omega s_1 \cdot \nabla\varphi \, dx - \frac{1}{2}\int_\Omega \nabla\sigma \cdot s_1 \varphi \, dx = 0. \tag{2.2}$$

Now define

$$J := \begin{bmatrix} 0 & -1 \\ 1 & 0 \end{bmatrix}.$$

Then, using the fact that the vector-valued function $\mathrm{e}^{-\sigma/2}s_1$ is a gradient, and that we are in two dimensions, we know that $J\nabla$ is a curl and therefore for any $\varphi \in H_0^1(\Omega)$

$$\int_\Omega \mathrm{e}^{-\sigma/2} J s_1 \cdot \nabla\varphi \, dx = 0.$$

This time replacing φ by $\mathrm{e}^{\sigma/2}\varphi$ in the above identity, we obtain for all $\varphi \in H^1_0(\Omega)$

$$\int_\Omega Js_1 \cdot \nabla\varphi \, dx + \frac{1}{2}\int_\Omega \nabla\sigma \cdot Js_1 \varphi \, dx = 0. \tag{2.3}$$

Using the fact that

$$\nabla\sigma = (\nabla\sigma \cdot s_1)\,\frac{s_1}{S_{11}} + (\nabla\sigma \cdot Js_1)\,\frac{Js_1}{S_{11}} \ \text{ a.e. in } \Omega,$$

for any $\Phi := (\varphi_1, \varphi_2) \in (C^1_c(\Omega))^2$ we obtain

$$\begin{aligned}
\frac{1}{2}\int_\Omega \sigma \mathrm{div}\,(\Phi)\, dx &= -\frac{1}{2}\int_\Omega \nabla\sigma \cdot \Phi \, dx \\
&= -\frac{1}{2}\int_\Omega (\nabla\sigma \cdot s_1)\,\frac{s_1}{S_{11}} \cdot \Phi \, dx - \frac{1}{2}\int_\Omega (\nabla\sigma \cdot Js_1)\,\frac{Js_1}{S_{11}} \cdot \Phi \, dx \\
&= -\int_\Omega s_1 \cdot \nabla\left(\frac{s_1}{S_{11}} \cdot \Phi\right) dx + \int_\Omega Js_1 \cdot \nabla\left(\frac{Js_1}{S_{11}} \cdot \Phi\right) dx, \qquad (2.4)
\end{aligned}$$

where we have used (2.2) with $\varphi := \Phi \cdot s_1/S_{11}$ and (2.3) with $\varphi := \Phi \cdot Js_1/S_{11}$. In both cases we have $\varphi \in H^1_0(\Omega)$, since this can be readily checked, using the assumption that $\nabla\sigma \in L^p(\Omega)$, $|\nabla u_1|^{-1} \in L^2(\Omega)$, and $|\nabla u_1|^{-2}\partial_{ij}u_1 \in L^2(\Omega)$.

Now note that the right-hand side of (2.4) depends only on the data s_1: therefore by choosing the support of Φ in ω, that is, where s_1 is known, we conclude that the left-hand side is known. This in turn proves that σ is known in ω up to an additive constant. ∎

We should observe that the assumptions on σ and $|\nabla u_1|$ in the above result are not of the same nature: σ is assumed to be sufficiently smooth, while ∇u_1 is assumed to be *away from zero*. Indeed this assumption depends on the boundary data but, as we shall see below, can be realized in some circumstances. For instance one may use classical regularity results in the following way to give an example in which the above assumptions are satisfied. First, by Morrey–Sobolev embedding theorem we know that for some $\alpha > 0$ we have $W^{1,p}(\Omega) \subset C^{0,\alpha}(\overline{\Omega})$, provided that $p > 2$ and $\Omega \subset \mathbb{R}^2$ is sufficiently smooth. Therefore, if we assume $\sigma \in W^{1,p}(\Omega)$, then $\mathrm{e}^\sigma \in C^{0,\alpha}(\overline{\Omega})$, and, assuming that the boundary data is sufficiently smooth, we conclude that $u \in C^{1,\alpha}(\overline{\Omega})$ (see, for instance, Theorems 8.32–8.33 in Gilbarg and Trudinger [6]). Now if we assume that Ω is convex, by the result of Theorem 1.1 we conclude that $|\nabla u_1| \neq 0$ in $\overline{\omega}$, and since $|\nabla u_1|$ is Hölder continuous, we have $|\nabla u_1|^{-1} \in L^\infty(\Omega)$, and the conditions of Proposition 2.1 are satisfied.

The proof of Proposition 2.1 uses the fact that two orthogonal projections of the flux s_1 can be related to the conductivity. In the next proposition we show that two distinct measurements, yielding three data S_{11}, S_{22}, and S_{12} allow us to recover the direction $\theta_1 := |\nabla u_1|^{-1}\nabla u_1$ up to a constant angle (and in turn, the conductivity using Proposition 2.1). This relies on the fact that, provided Ω is convex and smooth, if $g_1 = x_1$ and $g_2 = x_2$, then the solutions u_1, u_2 of (1.1) verify

$$\det(\nabla u_1, \nabla u_2) > 0 \text{ a.e. in } \omega, \tag{2.5}$$

thanks to Theorem 1.1.

Proposition 2.2. *Assume that Ω is convex and smooth, and that $g_1 = x_1$ and $g_2 = x_2$ so that (2.5) holds. Assume that S_{11}, S_{22}, and S_{12} are known in $\omega \subset \Omega$, and that u_1, u_2 satisfy (2.1). Then the direction*

$$\theta_1 := \frac{\nabla u_1}{|\nabla u_1|} = \frac{s_1}{|s_1|} = S_{11}^{-1/2} \mathrm{e}^{\sigma/2} \nabla u_1$$

is known up to a constant rotation.

Proof. First, note that $s_1 = \mathrm{e}^{\sigma/2}\nabla u_1$ and $s_2 = \mathrm{e}^{\sigma/2}\nabla u_2$ are related via two known functions of x. Indeed we may write for some $\alpha(x), \beta(x)$ that $s_2(x) = \alpha(x)s_1 + \beta(x)Js_1$ and since $\det(s_1, s_2) = s_1 \wedge s_2$ we have

$$s_2 = \alpha(x)s_1 + \beta(x)Js_1 = \frac{S_{12}}{S_{11}}s_1 + \frac{\det(s_1, s_2)}{S_{11}}Js_1. \tag{2.6}$$

The determinant $\det(s_1, s_2)$ is known, since thanks to (2.5) its sign is known to be positive (for instance), and therefore

$$\det(s_1, s_2) = \sqrt{S_{11}S_{22} - (S_{12})^2}.$$

From (1.1), we see that for $j = 1, 2$ we have $\operatorname{div}(\mathrm{e}^{\sigma/2}s_j) = 0$. Using (2.6) this means that for any compactly supported test function φ,

$$\int_\Omega \mathrm{e}^{\sigma/2} s_1 \cdot \nabla\varphi \, dx = 0, \tag{2.7}$$

$$\int_\Omega \mathrm{e}^{\sigma/2} \left(\alpha s_1 + \beta J s_1\right) \cdot \nabla\varphi \, dx = 0. \tag{2.8}$$

Note that $\mathrm{e}^{-\sigma/2}s_j$ is a gradient. Because $d = 2$, $J\nabla$ is a curl, and this implies

$$\int_\Omega \mathrm{e}^{-\sigma/2} Js_1 \cdot \nabla\varphi \, dx = 0, \tag{2.9}$$

$$\int_\Omega \mathrm{e}^{-\sigma/2} \left(\alpha J s_1 - \beta s_1\right) \cdot \nabla\varphi \, dx = 0. \tag{2.10}$$

For the second equation we used (2.6) to write $Js_2 = \alpha Js_1 - \beta s_1$. Assume momentarily that σ, s_1, and s_2 are smooth enough so that we can integrate by parts (2.8) and (2.10). Then using the fact that $\operatorname{div}(\mathrm{e}^{-\sigma/2}Js_1) = 0$, we obtain

$$\int_\Omega \mathrm{e}^{\sigma/2}\nabla\alpha \cdot s_1\varphi \, dx + \int_\Omega \mathrm{e}^{-\sigma/2}\nabla\left(\mathrm{e}^{\sigma}\beta\right) \cdot Js_1\varphi \, dx = 0$$

and

$$\int_\Omega \mathrm{e}^{-\sigma/2}\nabla\alpha \cdot Js_1\varphi \, dx - \int_\Omega \mathrm{e}^{\sigma/2}\nabla\left(\mathrm{e}^{-\sigma}\beta\right) \cdot s_1\varphi \, dx = 0.$$

Introducing $\mathcal{U} = (\nabla\alpha - J\nabla\beta)\beta^{-1}$, we have proved that

$$\int_\Omega \mathcal{U}\cdot s_1\varphi\,dx + \int_\Omega \nabla\sigma\cdot Js_1\varphi\,dx = 0 = \int_\Omega \mathcal{U}\cdot Js_1\varphi\,dx - \int_\Omega \nabla\sigma\cdot s_1\varphi\,dx. \tag{2.11}$$

Integrating by parts (2.7), we deduce from (2.11) the identity

$$-2\int_\Omega \operatorname{div}(s_1)\,\varphi\,dx = \int_\Omega \nabla\sigma\cdot s_1\varphi\,dx = \int_\Omega \mathcal{U}\cdot Js_1\varphi\,dx,$$

and, similarly, starting from (2.9), thanks to (2.11) we obtain

$$-2\int_\Omega \operatorname{div}(Js_1)\,\varphi\,dx = -\int_\Omega \nabla\sigma\cdot Js_1\varphi\,dx = \int_\Omega \mathcal{U}\cdot s_1\varphi\,dx.$$

Finally we have proved that for any $\Phi = (\varphi_1,\varphi_2)\in C_0^\infty(\Omega)^2$,

$$\begin{aligned}\int_\Omega \mathcal{U}\cdot J\Phi &= \int_\Omega (\mathcal{U}\cdot s_1)\left(\frac{J\Phi\cdot s_1}{S_{11}}\right) + (\mathcal{U}\cdot Js_1)\left(\frac{J\Phi\cdot Js_1}{S_{11}}\right)dx\\ &= -2\int_\Omega \left(\operatorname{div}(Js_1)\,\frac{J\Phi\cdot s_1}{S_{11}} + \operatorname{div}(s_1)\,\frac{J\Phi\cdot Js_1}{S_{11}}\right)dx\\ &= 2\int_\Omega \left(\operatorname{div}(Js_1)\,\frac{Js_1}{S_{11}} + \operatorname{div}(s_1)\,\frac{s_1}{S_{11}}\right)\cdot\Phi\,dx.\end{aligned}$$

A direct computation shows that if we set $\theta_1 := s_1/|s_1|$ and $\theta_1 = (\cos t, \sin t)$, we have

$$\int_\Omega \left(\operatorname{div}(Js_1)\,\frac{Js_1}{S_{11}} + \operatorname{div}(s_1)\,\frac{s_1}{S_{11}}\right)\cdot\Phi\,dx = \int_\Omega \left(-J\nabla t + \nabla(\log S_{11})\right)\cdot\Phi\,dx \tag{2.12}$$

or, equivalently,

$$\int_\Omega J\nabla t\cdot\Phi\,dx = -\int_\Omega \left(\operatorname{div}(Js_1)\,\frac{Js_1}{S_{11}} + \operatorname{div}(s_1)\,\frac{s_1}{S_{11}} - \nabla(\log S_{11})\right)\cdot\Phi\,dx. \tag{2.13}$$

Thus we have expressed ∇t in terms of known quantities. To conclude the proof, notice that with the regularity conditions assumed about u_1, u_2, σ, the integrals involving $\mathcal{U}$ and $\nabla(\log S_{11})$ are well defined, and therefore the function (or the angle) $t = t(x)$ is determined up to an additive constant. ∎

3. An optimal control approach. In section 2, we presented Propositions 2.1 and 2.2 to document the feasibility of the inversion in an ideal case. For the practical inversion, which will be discussed in what follows, we will adopt a very different approach. The inversion is considered as a minimization problem and is performed in two or three dimensions. In subsection 3.1, the minimization problems are precisely stated. The direct and adjoint differentiation of the cost functions is detailed in subsection 3.2. Such computations are relatively classical; see, e.g., [5] for an electric impedance tomography equivalent. Numerical simulations are presented in sections 5 and 6, where several boundary conditions are simultaneously considered

and the effective cost functions are the sum of cost functions similar to $\mathcal{J}_1$ or $\mathcal{J}_2$. Subsection 3.3 is devoted to the study of the convexity properties of the cost functions. We consider the general form (1.3) of the minimization problem and discuss the convexity properties of the minimization of

$$\mathcal{J}(\sigma) = \int_\Omega j\left(E(\sigma), x\right) dx. \tag{3.1}$$

As in (1.3), we assume that $j : \mathbb{R} \times \Omega \to L^1(\Omega)$ is a Caratheodory function which is C^2 with respect to its first variable, nonnegative, and such that $j(s,x) = 0$ if and only if $s = \mathrm{e}^{\sigma^\star(x)}|\nabla u_\star(x)|^2$, where $\mathrm{e}^{\sigma^\star}$ is the true conductivity and $u_\star$ is the associated electric potential. Strictly convex functionals are known to be favorable in optimization problems, as they imply uniqueness of the solution and convergence of descent algorithms. We show that the minimization is not fault free; namely, around the global minimizer, the Hessian of $\mathcal{J}$ is not positive definite.

3.1. The minimization problems. We assume that the true log-conductivity $\sigma^\star$ is known in a layer of positive thickness close to the boundary $\partial\Omega$. More precisely, we assume that $\sigma^\star$ is known in $\Omega \setminus \Omega'$, where Ω' is a subdomain such that $\mathrm{dist}(\Omega', \partial\Omega) > 0$. Let $g \in H^{1/2}(\partial\Omega)$. The set of admissible log-conductivities is

$$L^\infty_{\mathrm{ad}}(\Omega) = \{\sigma \in L^\infty(\Omega) \mid \sigma|_{\Omega\setminus\Omega'} = \sigma^\star\},$$

and its tangent space at any point is the subspace denoted by

$$L^\infty_0(\Omega) = \{\delta \in L^\infty(\Omega) \mid \delta|_{\Omega\setminus\Omega'} = 0\}.$$

If $\sigma \in L^\infty_{\mathrm{ad}}(\Omega)$, we denote by $u(\sigma) \in H^1$ the solution u of

$$\begin{cases} \nabla \cdot (\mathrm{e}^\sigma \nabla u) = 0 & \text{in } \Omega, \\ u = g & \text{on } \partial\Omega. \end{cases} \tag{3.2}$$

We describe two optimization methods for recovering the conductivity from energy density measurements. The heuristic idea is to find $\sigma \in L^\infty_{\mathrm{ad}}(\Omega)$ such that

$$E(\sigma) := \mathrm{e}^\sigma\, |\nabla u|^2$$

approaches $S = E(\sigma^\star)$. For the sake of concision we sometimes write $E(\sigma)$ instead of $E(\sigma, x) = \mathrm{e}^{\sigma(x)}|\nabla u(x)|^2$.

The first method uses local measurements of S on the subdomain ω: it consists of minimizing the cost function

$$\mathcal{J}_1(\sigma) = \int_\omega \left[\sqrt{E(\sigma)} - \sqrt{E(\sigma^\star)}\right]^2 dx. \tag{3.3}$$

This corresponds to the general problem (3.1) with $j(s,x) = (\sqrt{s} - \sqrt{E(\sigma^\star, x)})^2$ for $x \in \omega$ and $j(s,x) = 0$ otherwise.

The second method is a nested grids method. The domain Ω' is partitioned into subdomains $(\omega_i)_{1\le i\le n}$. Let $\omega_0 = \Omega \setminus \Omega'$. We assume that the total power in each ω_i $(i = 0, \dots, n)$ is known; this quantity is $\int_{\omega_i} E(\sigma^\star)$. The cost function to minimize is

$$\mathcal{J}_2(\sigma) = \frac{1}{2}\sum_{i=0}^{n}\left(\int_{\omega_i} E(\sigma)\,dx - \int_{\omega_i} E(\sigma^\star)\,dx\right)^2, \tag{3.4}$$

restricted to conductivities that are constant on each ω_i. Note that if a finite element method with piecewise constant conductivities on a mesh $(T_i)_{1\le i\le M}$ is used for the discretization of (3.1) with $j(s,x) = (s - E(\sigma^\star, x))^2$, then the minimization problem of (3.1) and the minimization of $\mathcal{J}_2$ are equivalent when $n = M$, and for all $i \in \{1, \dots, M\}$, $\omega_i = T_i$ if piecewise linear (P_1) finite elements are used.

To minimize these functionals, we shall use either a steepest descent algorithm with $\mathcal{J}_1$, or a Gauss–Newton algorithm with $\mathcal{J}_2$. Both approaches require differentiations.

3.2. Differentiation of $\mathcal{J}_1$ and $\mathcal{J}_2$. It is well known that the mapping $\sigma \mapsto u(\sigma)$ defined on $L^\infty_{\mathrm{ad}}(\Omega) \to H^1(\Omega)$ is C^∞ (in fact, analytic), and that if $\delta \in L^\infty_0(\Omega)$, the differential of u in the δ direction is $\mathrm{d}u.\delta = v$, where $v \in H^1_0(\Omega)$ is the solution of the variational problem

$$v \in H^1_0(\Omega), \quad \forall\, \varphi \in H^1_0(\Omega), \qquad \int_\Omega \mathrm{e}^\sigma \nabla v \cdot \nabla\varphi\,dx = -\int_\Omega \delta \mathrm{e}^\sigma \nabla u \cdot \nabla\varphi\,dx. \tag{3.5}$$

Consider the mapping

$$\begin{array}{rccc} E: & L^\infty_{\mathrm{ad}}(\Omega) & \longrightarrow & L^1(\Omega), \\ & \sigma & \longmapsto & \mathrm{e}^\sigma |\nabla u(\sigma)|^2. \end{array}$$

The mapping E is clearly differentiable, and its derivative in the δ direction is given by

$$\mathrm{d}E.\delta = \delta \mathrm{e}^\sigma |\nabla u|^2 + 2\mathrm{e}^\sigma \nabla u \cdot \nabla v, \tag{3.6}$$

where $v = \mathrm{d}u.\delta$ is the unique solution of (3.5).

Proposition 3.1. *The operator $\mathrm{d}E : L^\infty_0(\Omega) \to L^1(\Omega)$ has the following symmetry property: for all $\delta, \eta \in L^\infty_0(\Omega)$, denoting by $\langle\cdot,\cdot\rangle$ the duality between $L^1(\Omega)$ and $L^\infty(\Omega)$ we have*

$$\langle \mathrm{d}E.\delta, \eta\rangle = \langle \mathrm{d}E.\eta, \delta\rangle.$$

Proof. If $\eta \in L^\infty_0(\Omega)$, then

$$\mathrm{d}E.\eta = \eta \mathrm{e}^\sigma |\nabla u(\sigma)|^2 + 2\mathrm{e}^\sigma \nabla u(\sigma).\nabla w,$$

where w solves

$$\begin{cases} \nabla \cdot (\mathrm{e}^\sigma \nabla w) = -\nabla \cdot (\eta \mathrm{e}^\sigma \nabla u(\sigma)) & \text{in } \Omega, \\ w = 0 & \text{on } \partial\Omega. \end{cases} \tag{3.7}$$

We can write

$$\langle \mathrm{d}E.\delta, \eta\rangle_{L^1, L^\infty(\Omega)} = \int_\Omega \eta\delta \mathrm{e}^\sigma |\nabla u(\sigma)|^2 + 2\eta \mathrm{e}^\sigma \nabla u(\sigma) \cdot \nabla v.$$

The second term in this integral is evaluated by

$$\int_\Omega \eta \mathrm{e}^\sigma \nabla u(\sigma).\nabla v = -\int_\Omega v\nabla\cdot(\eta \mathrm{e}^\sigma \nabla u(\sigma)) = -\int_\Omega \mathrm{e}^\sigma \nabla v\cdot\nabla w.$$

As a result,

$$\langle \mathrm{d}E.\delta,\eta\rangle_{L^1,L^\infty(\Omega)} = \int_\Omega \eta\delta \mathrm{e}^\sigma |\nabla u(\sigma)|^2 - 2\int_\Omega \mathrm{e}^\sigma \nabla v\cdot\nabla w.$$

This quantity being symmetric in δ and η, it follows that

$$\langle \mathrm{d}E.\delta,\eta\rangle_{L^1,L^\infty(\Omega)} = \langle \mathrm{d}E.\eta,\delta\rangle_{L^1,L^\infty_0(\Omega),}$$

and the result is proved. ■

As a consequence of (3.5), if we write

$$\mathcal{J}_2(\sigma) = \frac{1}{2}||F(\sigma)||^2,$$

where

$$F(\sigma) = (f_i(\sigma))_{0\le i\le n}\in\mathbb{R}^{n+1} \quad \text{with} \quad f_i(\sigma) = \int_{\omega_i} E(\sigma) - \int_{\omega_i} E(\sigma^\star), \tag{3.8}$$

the mapping $F : L^\infty_{\mathrm{ad}}(\Omega)\to\mathbb{R}^{n+1}$ defined in (3.8) is differentiable, and if $\sigma\in L^\infty_{\mathrm{ad}}(\Omega)$ and $\delta\in L^\infty_0(\Omega)$,

$$\mathrm{d}F.\delta = (\mathrm{d}f_0.\delta,\mathrm{d}f_1.\delta,\dots,\mathrm{d}f_n.\delta),$$

with

$$\mathrm{d}f_i.\delta = \int_{\omega_i}\left(\delta + 2\frac{\nabla u(\sigma)\cdot\nabla v}{|\nabla u(\sigma)|^2}\right)\mathrm{e}^\sigma|\nabla u(\sigma)|^2\,dx, \tag{3.9}$$

where v solves (3.5).

Let us now study the adjoint differentiation of $\mathcal{J}_1$, and $\mathcal{J}_2$.

Proposition 3.2. *Assume that $\omega\subset\Omega'$. Let χ be the characteristic function of ω. Define an error function*

$$\varepsilon(\sigma) := \chi\mathrm{e}^\sigma\left(\sqrt{\frac{E(\sigma^\star)}{E(\sigma)}}-1\right),$$

and let p be the adjoint state solution of the variational problem

$$p\in H^1_0(\Omega),\quad \forall\,\varphi\in H^1_0(\Omega),\qquad \int_\Omega \mathrm{e}^\sigma\nabla p\cdot\nabla\varphi\,dx = \int_\Omega \varepsilon\nabla u\cdot\nabla\varphi\,dx.$$

The functional $\mathcal{J}_1$ is differentiable with respect to σ, and its derivative is given by

$$\mathrm{d}\mathcal{J}_1.\delta = \int_\Omega \delta\left(-\varepsilon + 2\frac{\nabla u\cdot\nabla p}{|\nabla u|^2}\right)\mathrm{e}^\sigma|\nabla u|^2\,dx. \tag{3.10}$$

Proof. Note that $p \in H^1_0(\Omega)$ is the solution to the elliptic adjoint problem $\operatorname{div}(\mathrm{e}^\sigma \nabla p) = \operatorname{div}(\varepsilon(\sigma)\nabla u)$. We have

$$\mathcal{J}_1(\sigma) = \int_\Omega \chi \left(\sqrt{E(\sigma)} - \sqrt{E(\sigma^\star)}\right)^2 dx,$$

and so the derivative of $\mathcal{J}_1$ is

$$\mathrm{d}\mathcal{J}_1.\delta = \int_\Omega \chi \left(\sqrt{E(\sigma)} - \sqrt{E(\sigma^\star)}\right) \left(\delta \mathrm{e}^{\sigma/2}|\nabla u| + 2\mathrm{e}^{\sigma/2}\frac{\nabla v \cdot \nabla u}{|\nabla u|}\right) dx, \tag{3.11}$$

where $v = \mathrm{d}u.\delta$ is defined in (3.5). In order to write the derivative $\mathrm{d}\mathcal{J}_1$ in terms of δ only—and not in terms of δ and v—an adjoint problem is used. Namely, let $p \in H^1_0$ be the solution of

$$\begin{aligned} &p \in H^1_0(\Omega), \quad \forall\, \varphi \in H^1_0(\Omega), \\ &\int_\Omega \mathrm{e}^\sigma \nabla p \cdot \nabla \varphi \, dx = -\int_\Omega \chi \left(\sqrt{E(\sigma)} - \sqrt{E(\sigma^\star)}\right) \mathrm{e}^{\sigma/2}\frac{\nabla u \cdot \nabla \varphi}{|\nabla u|}\, dx \\ &\qquad\qquad = \int_\Omega \varepsilon \nabla u \cdot \nabla \varphi \, dx. \end{aligned} \tag{3.12}$$

Then, choosing $\varphi := v$ in (3.13), it follows from (3.5) with $\varphi = p$ that

$$\mathrm{d}\mathcal{J}_1.\delta = \int_\Omega \left(\chi \mathrm{e}^\sigma |\nabla u|^2 \left(1 - \sqrt{E(\sigma^\star)/E(\sigma)}\right) + 2\mathrm{e}^\sigma \nabla u \nabla p\right) \delta \, dx,$$

which is (3.10). ∎

Proposition 3.3. *Let $\sigma \in L^\infty_{\mathrm{ad}}(\Omega)$ and $Z = (z_0, z_1, \dots, z_n) \in \mathbb{R}^{n+1}$. Then*

$$\mathrm{d}F^T.Z = z|\nabla u|^2 + 2\nabla u \cdot \nabla p\,, \tag{3.13}$$

where z is the piecewise constant function equal to z_i in ω_i $(i = 0, \dots, n)$ and p solves

$$\begin{cases} \nabla \cdot (\mathrm{e}^\sigma \nabla p) = \nabla \cdot (z\mathrm{e}^\sigma \nabla u) & \text{in } \Omega, \\ p = 0 & \text{on } \partial\Omega. \end{cases} \tag{3.14}$$

This, for instance, allows us to compute the gradient of the cost function $\mathcal{J}_2$. Indeed, since $\mathcal{J}_2(\sigma) = \frac{1}{2}||F||^2$ we have

$$\nabla \mathcal{J}_2 = \mathrm{d}F^T.F,$$

and so it suffices to apply (3.13) with $Z = F$.

Proof of Proposition 3.3. If $\delta \in L^\infty_0(\Omega)$, then

$$\langle \mathrm{d}F^T.Z, \delta\rangle_{L^1, L^\infty(\Omega)} = \langle Z, \mathrm{d}F.\delta\rangle_{\mathbb{R}^{n+1}} = \sum_{i=0}^n z_i \int_{\omega_i} \delta \mathrm{e}^\sigma |\nabla u|^2 + 2\mathrm{e}^\sigma \nabla u \cdot \nabla v \, dx.$$

Using the definition of z this can be written as

$$\left\langle \mathrm{d}F^T.Z, \delta\right\rangle_{L^1, L^\infty_0(\Omega)} = \int_\Omega z\delta \mathrm{e}^\sigma |\nabla u(\sigma)|^2 + 2z\mathrm{e}^\sigma \nabla u(\sigma) \cdot \nabla v \, dx.$$

Let us evaluate the second term on the right-hand side. Choosing v as a test function in the adjoint equation satisfied by p, and choosing p as a test function in the equation satisfied by v, we have

$$\int_\Omega z\mathrm{e}^\sigma \nabla u(\sigma)\cdot\nabla v\,dx = \int_\Omega \mathrm{e}^\sigma \nabla p\cdot\nabla v\,dx = \int_\Omega \delta \mathrm{e}^\sigma \nabla p\cdot\nabla u\,dx.$$

Hence for every $\delta\in L_0^\infty(\Omega)$,

$$\langle \mathrm{d}F^T.Z,\delta\rangle_{L^1,L^\infty(\Omega)} = \int_\Omega \left(z\mathrm{e}^\sigma|\nabla u|^2 + 2\mathrm{e}^\sigma\nabla u\cdot\nabla p\right)\delta\,dx. \qquad \blacksquare$$

3.3. Local minimizers and degenerate convexity. We make the following simple observation.

Proposition 3.4. *Assume that σ is such that $E(\sigma)=E(\sigma^\star)$. Then*

$$\left|D^2\mathcal{J}(\sigma)\cdot[\delta,\delta]\right| \le 2\left\|\frac{d^2j}{ds^2}(E(\sigma^\star),x)\,E(\sigma^\star)\right\|_\infty D^2\mathcal{J}_1(\sigma)\cdot[\delta,\delta], \tag{3.15}$$

and whenever $|\frac{d^2j}{ds^2}(E(\sigma^\star),x)|^{-1}$ is integrable we have

$$\left(\int_\Omega \left|\frac{d^2j}{ds^2}(E(\sigma^\star),x)\right|^{-1}dx\right)^{-1}\left(\int_\Omega E\delta dx\right)^2 \le D^2\mathcal{J}\cdot[\delta,\delta]. \tag{3.16}$$

When $\mathcal{J}=\mathcal{J}_1$, we have

$$\frac12\left(\int_\Omega E(\sigma^\star)\,dx\right)^{-1}\left(\int_\Omega E(\sigma^\star)\,\delta dx\right)^2 \le D^2\mathcal{J}_1(\sigma)\cdot[\delta,\delta] \le \frac12\int_\Omega E(\sigma^\star)\,\delta^2\,dx.$$

Note that Proposition 3.4 illustrates the fact that it is sufficient to study the case $\mathcal{J}=\mathcal{J}_1$ to prove that degeneracy in the convexity is general. In particular, inequality (3.15) shows that the Hessian of $\mathcal{J}$ cancels simultaneously with that of $\mathcal{J}_1$ if the energy density is smooth.

The lower bound (3.16) does not prove strict convexity. However, it provides a rule-of-thumb on how to mend steepest descent algorithm resolutions that tend to stall close to the minimizer. Since $E(\sigma^\star)$ is strictly positive, the lower bound will not vanish if $\delta\ge 0$, or $\delta\le 0$ everywhere. Therefore, if $\delta^\star$ is the increment given by the algorithm, choosing to alternately apply either $\max(\delta^\star,0)$ or $\min(\delta^\star,0)$ will avoid a degenerate behavior.

Proof of Proposition 3.4. Performing the same computation as in the proof of Proposition 3.2, we have for $\sigma\in L^\infty_{\mathrm{ad}}(\Omega)$ and $\delta\in L_0^\infty(\Omega)$

$$D\mathcal{J}(\sigma)\cdot\delta = \int_\Omega \frac{\partial j}{\partial s}(E(\sigma),x)\,E(\sigma)\left[\delta + 2\frac{\nabla v\cdot\nabla u}{|\nabla u|^2}\right]dx.$$

Another differentiation shows that the second derivative is given by

$$\begin{aligned} D^2\mathcal{J}(\sigma)\cdot[\delta,\delta] = &\int_\Omega \frac{\partial^2 j}{\partial s^2}(E(\sigma),x)\left[E(\sigma)\left(\delta+2\frac{\nabla v\cdot\nabla u}{|\nabla u|^2}\right)\right]^2 dx \\ &+\int_\Omega \frac{\partial j}{\partial s}(E(\sigma),x)\,E(\sigma)\left[\delta^2+4\delta\frac{\nabla v\cdot\nabla u}{|\nabla u|^2}+2\frac{\nabla w\cdot\nabla u}{|\nabla u|^2}\right]dx, \end{aligned}$$

where $w \in H_0^1(\Omega)$ is the second derivative of $u(\sigma)$ in the direction δ. When $\dfrac{\partial j}{\partial s}(E(\sigma), x) \equiv 0$, that is, at a critical point of $\mathcal{J}$, this simplifies as

$$D^2\mathcal{J}(\sigma)\cdot[\delta,\delta] = \int_\Omega \frac{d^2 j}{ds^2}(E(\sigma),x)\left[E(\sigma)\left(\delta + 2\frac{\nabla v\cdot\nabla u}{|\nabla u|^2}\right)\right]^2 dx. \tag{3.17}$$

Note that at the global minimizer, that is, when $E(\sigma) = E(\sigma^\star)$ a.e. in ω, by construction identity (3.17) holds and $\frac{\partial^2 j}{\partial s^2}(E(\sigma),x) \geq 0$. Therefore,

$$\begin{aligned}\left|D^2\mathcal{J}(\sigma)\cdot[\delta,\delta]\right| &\leq \left\|\frac{d^2 j}{ds^2}(E(\sigma^\star),x)\,E(\sigma^\star)\right\|_\infty \int_\omega E(\sigma)\left[\delta + 2\frac{\nabla v\cdot\nabla u}{|\nabla u|^2}\right]^2 dx\\ &\leq 2\left\|\frac{\partial^2 j}{\partial s^2}(E(\sigma^\star),x)\,E(\sigma^\star)\right\|_\infty D^2\mathcal{J}_1(\sigma)\cdot[\delta,\delta],\end{aligned}$$

upon applying formula (3.17) to

$$j(s,x) = \left(s^{1/2} - E(\sigma^\star,x)^{1/2}\right)^2.$$

This proves the first part of the proposition. Let us now turn to $\mathcal{J}_1$. Expanding $D^2\mathcal{J}_1(\sigma)\cdot[\delta,\delta]$, we find

$$\begin{aligned}D^2\mathcal{J}_1(\sigma)\cdot[\delta,\delta] &= \frac{1}{2}\int_\Omega E(\sigma)\delta^2\,dx + 2\int_\Omega E(\sigma)\left[\frac{\nabla v\cdot\nabla u}{|\nabla u|^2}\right]^2 dx\\ &\quad + 2\int_\Omega \delta\nabla u\cdot\nabla v\,dx,\\ &= \frac{1}{2}\int_\Omega E(\sigma)\delta^2\,dx + 2\int_\Omega \frac{e^\sigma}{|\nabla u|^2}\Big([\nabla v\cdot\nabla u]^2 - |\nabla v|^2|\nabla u|^2\Big)dx,\end{aligned}$$

where we have used (3.5) with $\varphi = v$. Since, by the Cauchy–Schwarz inequality, the second term on the right-hand side is nonpositive, we have shown that

$$D^2\mathcal{J}_1(\sigma)\cdot\delta\cdot\delta \leq \frac{1}{2}\int_\Omega E(\sigma)\delta^2\,dx.$$

On the other hand, if we choose v as a test function in (3.2) and integrate by parts, we obtain

$$\int_\Omega E(\sigma)\frac{\nabla v\cdot\nabla u}{|\nabla u|^2}\,dx = 0.$$

As a consequence,

$$\begin{aligned}\left(\int_\Omega E(\sigma)\,\delta\,dx\right)^2 &= \left(\int_\Omega E(\sigma)\left[\delta + 2\frac{\nabla v\cdot\nabla u}{|\nabla u|^2}\right]dx\right)^2\\ &\leq D^2\mathcal{J}\cdot[\delta,\delta]\left(2\int_\Omega E(\sigma)\,dx\right),\end{aligned}$$

using again the Cauchy–Schwarz inequality. ∎

The next proposition shows that the Hessian $D^2\mathcal{J}$ is not always positive definite. We provide a counterexample in the simplest case, that is, for the Laplacian.

Proposition 3.5. *Let $\Omega := (0,\pi)^2$. Assume that $\sigma \equiv 0$, while $g = x_1$, and $\partial j/\partial s\,(E\,(0)\,,x) \equiv 0$. Then there exist directions δ such that*

$$\|\delta\|_{L^2(\Omega)} = 1 \quad \textit{and} \quad D^2\mathcal{J}\,(0)\,[\delta,\delta] = 0.$$

Proof. Since $\sigma = 0$, we have $u := u_1 = x_1$. The corrector $v \in H_0^1$ given by (3.5) satisfies

$$\Delta v = -\nabla_x \delta. \tag{3.18}$$

Choose

$$\begin{aligned}\delta(x,y) &= \sum_{n=1}^{\infty} 2d_n \cos(nx)\sin(ny)\\ &= \sum_{n=1}^{\infty} d_n \sin(n(x+y)) + \sum_{n=1}^{\infty} d_n \sin(n(y-x)),\end{aligned}$$

with

$$\frac{\pi}{2}\sum_{n=1}^{\infty} d_n^2 = 1.$$

An explicit computation gives

$$v(x,y) = -\sum_{n=1}^{\infty} \frac{1}{2n} d_n \sin(nx)\sin(ny)$$

and

$$\delta + 2\frac{\nabla u\cdot\nabla v}{|\nabla u|^2} = 0 \text{ in } \Omega.$$

Therefore, since from formula (3.17) we have

$$D^2\ \mathcal{J}(0)[\delta,\delta] = \frac{1}{2}\int_\Omega \frac{d^2 j}{ds^2}\,(E(0),x)\left[E(0)\left(\delta + 2\frac{\nabla u\cdot\nabla v}{|\nabla u|^2}\right)\right]^2 dx,$$

the proof is complete. ∎

Remark. In the proof of Proposition 3.5, we selected an ad hoc family of perturbations to cancel the Hessian. Had we started with a perturbation of the general form

$$\delta = \sum_{n\geq 0}\sum_{p>0} d_{n,p}\cos(nx)\sin(py),$$

we would have obtained

$$\left(\delta + 2\frac{\nabla u\cdot\nabla v}{|\nabla u|^2}\right)^2 = \sum_{p>0} d_{0,p}^2 \sin^2(py) + \sum_{n>0,p>0} d_{n,p}^2\left(\frac{n^2-p^2}{n^2+p^2}\right)^2 \cos^2(nx)\sin^2(py).$$

The first sum on the right-hand side corresponds to the Hessian along the $\nabla u/|\nabla u| = (1,0)$ direction. These terms are not weighted by any attenuation factor. Therefore the increment in a steepest descent algorithm is the most important in that direction. This, we think, is an explanation for the speedup observed in computations when multiple currents are used, simultaneously or alternately: the optimization becomes efficient in multiple directions.

4. Minimization of the cost function $\mathcal{J}_2$. This section is dedicated to the presentation of the minimization algorithm for $\mathcal{J}_2$. We do not detail the gradient descent—or steepest descent—algorithm used for $\mathcal{J}_1$. It is a steepest descent algorithm with an adaptive step that was implemented using `FreeFem++` [8]. Several boundary conditions are used to estimate the conductivity: $g_1, \dots, g_N$. The cost function is the sum of the cost functions associated to these boundary conditions: $\mathcal{J}_1 = \sum_{1\le k\le N} \mathcal{J}_1^k$. Note that the positivity constraint for the conductivity is automatically satisfied by the choice of a log-conductivity ($e^\sigma > 0$).

The optimization procedures used to minimize the cost function $\mathcal{J}_2$ are detailed. Although we always use the Gauss–Newton method, a different approach is followed for fine or coarse computations, which yields in turn a nested grid algorithm, presented in section 4.2.

4.1. Gauss–Newton optimization. We make use of several boundary conditions to estimate the conductivity: $g_1, \dots, g_N$. The cost function is the sum of the cost functions associated to these boundary conditions: $\mathcal{J}_2 = \sum_{1\le k\le N} \mathcal{J}_2^k$.

The domain Ω is divided into subdomains $(\omega_i)_{0\le i\le n}$. The true value of the conductivity in ω_0 is assumed to be known. We consider $F : \mathbb{R}^n \to (\mathbb{R}^n)^N$, $\sigma \mapsto (F_1(\sigma), \dots, F_N(\sigma))$, where F_k is associated to the boundary condition g_k and is defined as in (3.8). The map F is C^1 and $\mathrm{d}F = (\mathrm{d}F_1, \dots, \mathrm{d}F_N)$.

The Gauss–Newton method is an iterative descent method designed to minimize a cost function of the form

$$\mathcal{J}_2(\sigma) = \frac{1}{2}||F(\sigma)||^2 = \sum_{k=1}^{N} ||F_k(\sigma)||^2.$$

An initial guess σ^0 is provided, and the mth iteration reads as $\sigma^{m+1} := \sigma^m + \delta^m$, where the descent direction δ^m solves

$$\mathrm{d}F^T.\mathrm{d}F.\delta^m = -\mathrm{d}F^T.F. \tag{4.1}$$

If the number n of unknowns is small (typically n smaller than 20), the Jacobian matrices $\mathrm{d}F_k$ are computed columnwise by solving n conductivity problems using formula (3.9). Equation (4.1) is then assembled and solved easily using any linear solver since $\mathrm{d}F^T.\mathrm{d}F = \sum_{k=1}^N \mathrm{d}F_k^T.\mathrm{d}F_k$ and $\mathrm{d}F^T.F = \sum_{k=1}^N \mathrm{d}F_k^T.F_k$.

The step δ^m obtained is used as is, without further modification. If the number of unknowns n is large (for a fine spatial resolution there can be one unknown value of the conductivity in each convex element on the finite element mesh), the computation of the full matrix $\mathrm{d}F$ is time and memory consuming. We use an iterative method, namely, the conjugate gradient, to solve (4.1) without assembling $\mathrm{d}F$. This requires merely the knowledge of the right-hand side $\mathrm{d}F^T.F$ and a procedure that gives the product of the matrix $\mathrm{d}F^T.\mathrm{d}F$ by a given vector. These are provided by the direct and adjoint differentiations described in section 3.2.

More precisely, $F(\sigma^m)$ is computed by solving N conductivity problems; $\mathrm{d}F^T.F$ is computed by adjoint differentiation (N adjoint problems of conductivity to be solved); and if ξ is given, $\mathrm{d}F^T.\mathrm{d}F\xi = \mathrm{d}F^T.(\mathrm{d}F.\xi)$ is computed in two steps, solving N direct then N adjoint conductivity problems.

We implemented the algorithms that are sketched below.

Algorithm 1. Multiple subdomain conductivity estimation (full Jacobian).

input: *the values of the boundary currents* $g_1, \dots, g_N$ *and the associated measurements* $E_1(\sigma^\star), \dots, E_N(\sigma^\star)$, *initial guess* σ^0 *(such that* $\sigma^0 = \sigma^\star$ *in* $\Omega \setminus \omega$*)*

1. set $m := 0$;
2. compute the potentials $u_1, \dots, u_N$ predicted with the log-conductivity σ^m;
3. compute $F_k = (f_{k,1}, f_{k,2}, \dots, f_{k,n})$, where $f_{k,i} = \int_{\omega_i} \mathrm{e}^{\sigma^m} |\nabla u_k|^2 - \int_{\omega_i} E_k(\sigma^\star)$, for $k = 1 \dots, N$;
4. compute $\mathrm{d}F_k$, $k = 1 \dots, N$, columnwise using (3.9);
5. solve for δ the equation $(\sum_{1 \le k \le N} \mathrm{d}F_k^T.\mathrm{d}F_k)\delta = -\sum_{1 \le k \le N} \mathrm{d}F_k^T.F_k$;
6. update the log-conductivity: $\sigma^{m+1} := \sigma^m + \delta$;
7. if the stopping criterion is not met, set $m := m + 1$ and go to step 2.

Algorithm 2. Fine conductivity estimation (zero memory).

Same as Algorithm 1 above except

4. compute $\mathrm{d}F_k^T.F_k$, $k = 1 \dots, N$, using (3.13);
5. solve for δ the equation $(\sum_{1 \le k \le N} \mathrm{d}F_k^T.\mathrm{d}F_k)\delta = -\sum_{1 \le k \le N} \mathrm{d}F_k^T.F_k$, using conjugate gradient.

4.2. Nested grids identification of the conductivity. The conductivity distribution is retrieved from $E_1(\sigma^\star), \dots, E_N(\sigma^\star)$ by the following nested grids algorithm that is a combination of Algorithms 1 and 2. We refer to this approach as a "nested grids" approach rather than a "nested grid" approach, even though multiple grids are used, in order to avoid confusion with what is usually referred to as multigrid [7]. In particular, no use is made of the potentials on coarser grids to evaluate potentials on finer ones.

Algorithm 3. Combined algorithm.

input: *the discretization mesh, the values of the boundary currents* $g_1, \dots, g_N$ *and the associated measurements* $E_1(\sigma^\star), \dots, E_N(\sigma^\star)$, *initial guess for the log-conductivity*

1. set $n := 1$, set $\omega_1 = \omega$, estimate the log-conductivity σ provided by Algorithm 1;
2. define a new partition of Ω by dividing each $(\omega_i)_{1 \le i \le n}$ into two subdomains (that are unions of convexes of the mesh); set $n := 2n$;
3. find an optimal log-conductivity σ that is constant in each ω_i using Algorithm 1;
4. if $n > 20$, go to step 5; else go to step 2;
5. the partition of Ω is the partition defined by the convexes of the mesh;
6. find the log-conductivity σ that is constant in each convex using Algorithm 2.

5. Numerical results using the cost function $\mathcal{J}_1$. In this section, we document the efficiency of the reconstruction method using $\mathcal{J}_1$. A steepest descent algorithm with adaptive step was implemented using `FreeFem++` [8] for the minimization of $\mathcal{J}_1$ (however, we do not detail this gradient descent—or steepest descent—algorithm). Several boundary conditions $g_1, \dots, g_N$ are used to estimate the conductivity. The cost function is the sum of the cost functions associated to these boundary conditions: $\mathcal{J}_1 = \sum_{1 \le k \le N} \mathcal{J}_1^k$.

Note that in contrast with the theoretical reconstruction done in section 2, we only make use of the diagonal data, that is, S_{ii}, $i = 1, \dots, N$, and we make no assumption on the regularity of these data.

We study a test case that was introduced in [2]. On a disk of diameter 8, different conductivities are set: the background conductivity is equal to 0.5, the conductivity in the small disk to 0.75, the one in the triangle to 0.15, and finally the one in the L-shaped domain to 2.55 (see Figure 2). On the annulus of inner radius 6 and outer radius 8, the conductivity is supposed known, equal to 0.5. Dirichlet boundary data are fixed to be equal to the Cartesian coordinates $g_1 = x$, $g_2 = y$, $g_3 = x + y$, and $g_4 = x - y$ on the boundary of the circle.

Note that $S_{33} = S_{11} + S_{22} + 2S_{12}$ and $S_{44} = S_{11} + S_{22} - 2S_{12}$. Hence the knowledge of this set of four data is actually equivalent to the knowledge of the hypothesis of the theoretical reconstruction done in section 2.

5.1. The whole domain. The first reconstruction test is performed with $\omega = \Omega$; that is, S_{ii}, $i = 1, \dots, 4$, is known everywhere. The reconstruction experiments are conducted in three different cases. The first case is intended to document the convergence of the algorithm in a very favorable situation. The same mesh is used to compute the reconstruction and to obtain the synthetic data. This mesh is a 50K structured triangulation adapted to the shape of the inhomogeneities. We then consider the same synthetic data, but no a priori information is contained in the reconstruction mesh. We use a uniform Delaunay mesh of the ball of 110K triangles. A third test is performed with two different meshes, and a fourth test where the synthetic data is perturbed by a 10% multiplicative random noise. Finally, we test the effect of subsampling, that is, when only partial averaged data is available.

Our initial guess for the conductivity inside the inner circle of radius 6 was 1—any arbitrary number would do as well. Convergence curves are reported in Figure 3. For each of the three cases, we represent the evolution of the functional $\mathcal{J}_1$ to be minimized (on the left) and the L^1 error of σ_{comp}, the computed log-conductivity compared to $\sigma^\star$, the target log-conductivity (on the right). In practical applications, the correct conductivity is unknown: it is presented here to document the efficiency of the algorithm.

The test with a single mesh was performed to verify the convergence of the algorithm to the correct minimizer in an ideal situation. The evolution of the objective function and of the L^1 error toward machine precision leaves no doubt about the efficiency of the scheme. When the meshes are different, or when noise is added, the reconstruction is naturally less precise. In Figure 4 the absolute value of the relative differences between the computed and synthetic conductivity are plotted. The greyscale used varies between 0% and 10%.

In the noiseless cases (left), the plot clearly shows that the conductivity is recovered inside the shapes and on the background. The error is located only on the boundaries of the inclusions. This could be an effect of the mesh, since the boundaries cross the reconstruction

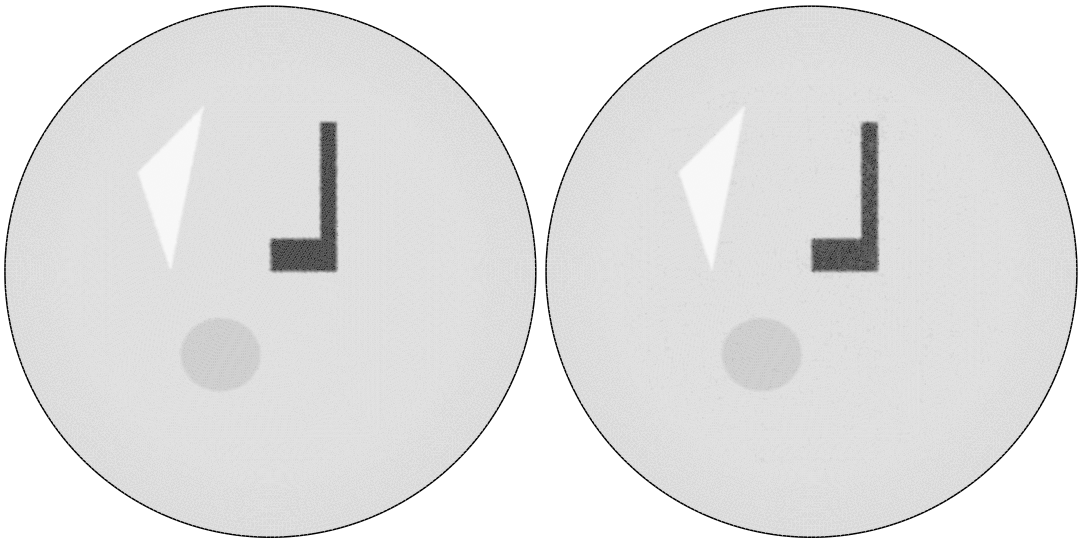

Figure 2. *The reference material (left) and the reconstruction with* 10% *noise (right). The conductivities are* 0.5 *for the background,* 0.15 *for the triangle,* 0.75 *for the disc, and* 2.55 *for the L-shaped region. The computations were done using* `FreeFem++`*, with xd3d for the rendering.*

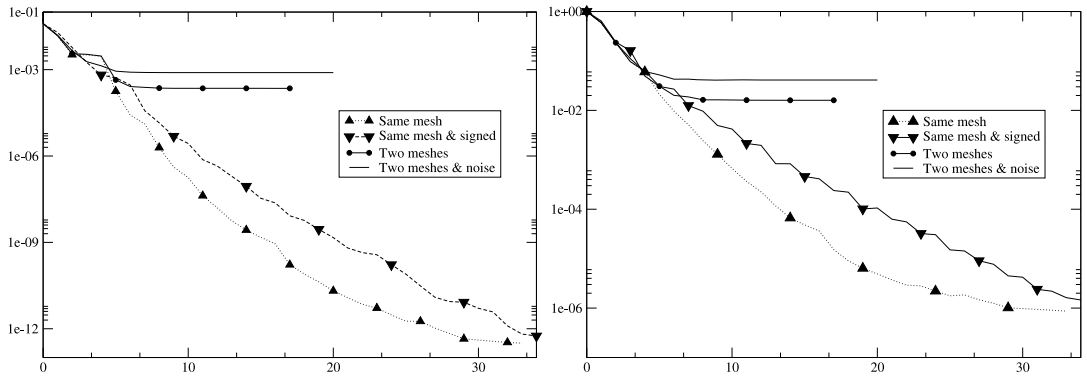

Figure 3. *Convergence histories for the whole domain. The objective function* $\mathcal{J}_1$ *is on the left, and the* L^1 *norm of the true error in conductivity is on the right. The dotted, triangle up, curve is for the one mesh noiseless case. The dashed, triangle down, curve corresponds to the case when only positive or negative increments are considered at each step. The solid line with disks corresponds to a reconstruction on a uniform mesh, with no added noise, and the plain solid line is for a uniform mesh and* 10% *noise.*

mesh in a nonconformal way. Figure 4 (left) also shows that shape corners create discrepancies. Around these points, the correct potential is singular, whereas the reconstructed potential inherits additional smoothness from the uniform mesh.

When noise is added, Figure 4 (right) shows that a 10% multiplicative noise leads to a relative loss of precision in the conductivity of about 10%, which is the best one can expect.

In section 3.3, it was mentioned that to avoid loss of convexity in the descent, one could choose to pick, at each iteration, either the positive direction $\delta_+ = \max(\delta, 0)$ or the negative one $\delta_- = \min(\delta, 0)$. We show the result in Figure 3, for one mesh, when $\delta_\pm$ is picked if its L^2

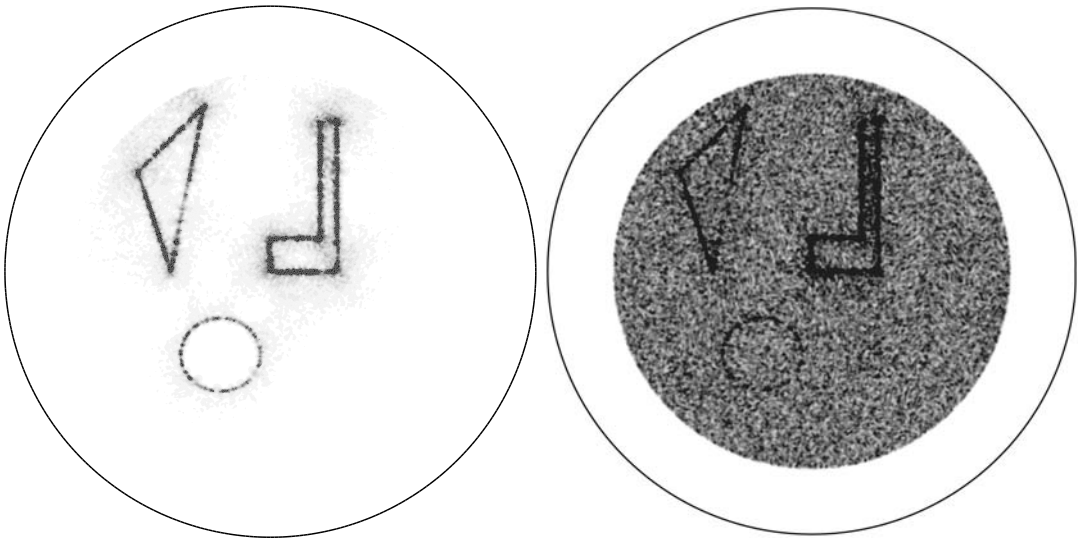

Figure 4. *The absolute relative difference for the conductivity for the whole domain without noise (left) or with a* 10% *multiplicative noise (right). The white areas correspond to a* 0% *error, and the black ones to a* 10% *error or more.*

norm is the largest. The rate of convergence is similar to the one observed before. If instead δ_+ (resp., δ_-) is used every other iteration, the convergence curve is more step-like, but the overall rate is comparable.

Note that this reconstruction method is slower than the one in [2]. However, because it is based on a minimization approach, it is more stable. Additionally, it requires only one current data set, whereas the method presented in [2] cannot be used in that case.

We also tested the effect of interpolation error, in the spirit of the examples presented in [2]. The data is first synthesized on a fine adapted mesh. It is then interpolated on a coarser uniform mesh. It is then reconstructed on a finer, but uniform, mesh. The coarser mesh is a 20K triangle Delaunay mesh of a ball. This test amounts to averaging the data; it corresponds to the physical situation where the average of the density of energy on small sets is measured and not the pointwise energy. As can be seen in Figure 5, the reconstruction is satisfying. It is to be compared with the coarse mesh interpolation of conductivity, displayed in the left-hand image.

5.2. Measurements in a smaller domain, and dependence on the outer domain. We then tested the case when the energy density data was available only in an ellipse ω around the L-shaped domain. The reconstruction is shown in Figure 6 (left). Again, the resulting conductivity closely approaches the reference one. This test validates the capacity of the algorithm to focus on smaller patches, hence having the ability to zoom in on a region of interest. The mesh used for this test is adapted to the ellipse: it is refined inside the ellipse and uniform outside. An interesting feature of this test is the tendency of the algorithm to compensate for discrepancies of the conductivity outside ω within a boundary layer in the neighborhood of ω. A close look at Figure 6 (left) shows that the higher conductivity on the left boundary of the ellipse stands for the triangle, and the one on the upper side is the upper

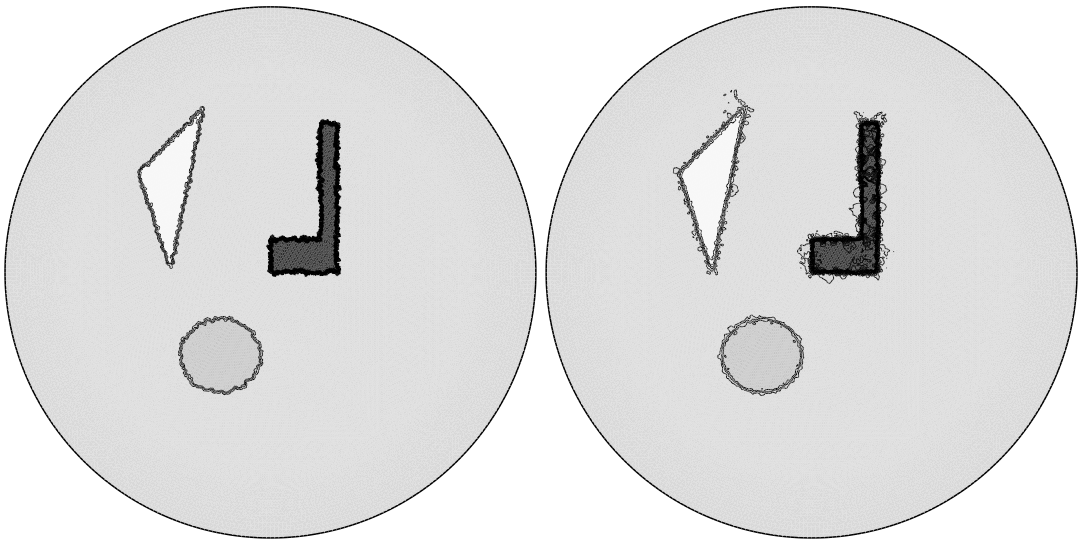

Figure 5. *Interpolation of the data on a coarser mesh: the interpolation of the conductivity (left) and the computed conductivity (right).*

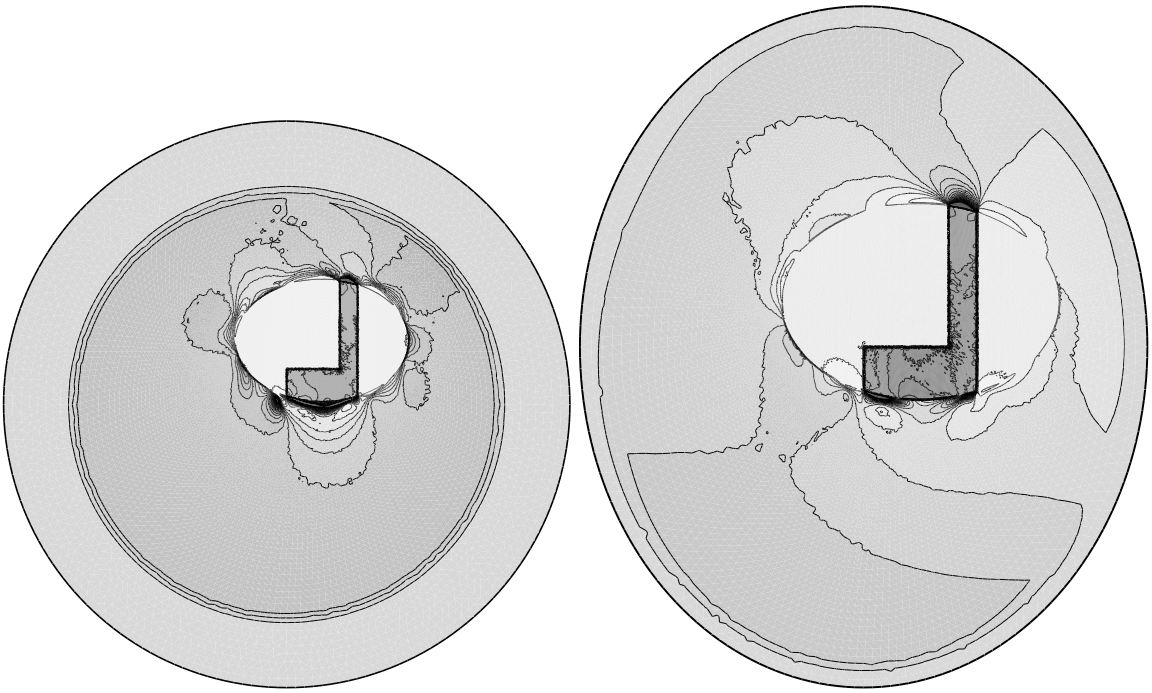

Figure 6. *Reconstruction from partial data. On the left, the reconstruction inside an elliptic region, with the whole domain thoroughly known. On the right, the reconstruction when the domain outside the ellipse is changed, with the same data as on the left.*

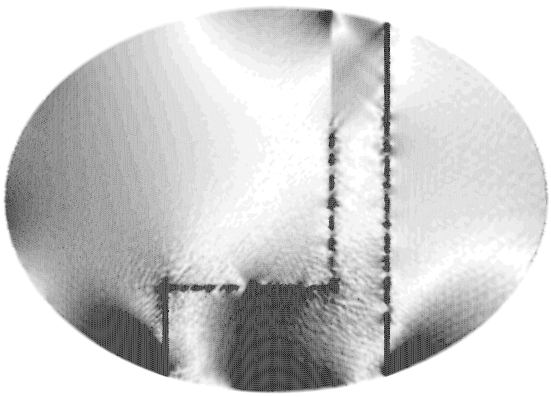

Figure 7. *Absolute relative difference between the synthetic data and the reconstructed conductivity shown in Figure 6 (right). The reconstructed conductivity is rescaled by a* 1.72 *factor. The white areas correspond to* 0% *error, and the black ones to a* 10% *error or more.*

branch of the L-shape that is not contained in the ellipse. Note that the computed conductivity is found only up to a multiplicative constant. This corroborates the study done in section 2, for more regular conductivities.

A natural question is whether such a reconstruction is still possible when the domain Ω and the Dirichlet boundary data g_i are only approximately known. This is of practical importance, because for in vivo experiments, the exact geometry of the boundary, the human body, is not precisely known.

In this test, the elliptic measurement subdomain is preserved, but we attempt to recover σ with a domain Ω that has been changed into a smaller ellipse. The Dirichlet boundary data imposed are the Cartesian coordinate data g_i previously used, x, y, $x+y$, $x-y$, but they are now imposed on this new domain. Because they are not the $e^{\sigma^\star}$-harmonic extensions of the previous boundary conditions, an error is introduced in the boundary conditions.

The resulting computed conductivity σ_{comp} is given in Figure 6 (right).

The absolute relative error between the computed conductivity and the synthetic data inside the ellipse is shown in Figure 7, on a greyscale between 0% and 10%. Note that since the conductivity is recovered up to a constant, the result was rescaled by a multiplicative factor (1.72) for the comparison. In this example, 89% of the area corresponds to less than 10% relative error.

5.3. Solving with a patchwork approach. The previous tests show that the conductivity can be recovered within a "patch," a subregion of the domain. We now investigate whether the algorithm can be parallelized with multiple computers recovering different patches. Since no constraint is imposed on the conductivity outside the area of interest, Figure 6 shows that the minimization procedure tends to create important errors outside the optimized patch ω, in a boundary layer surrounding ω. Furthermore, it reconstructs the conductivity up to a constant factor, which a priori depends on the subregion. A natural concern is whether these errors would render parallelization inefficient.

The following numerical trial is an attempt to address this question. Given two overlapping

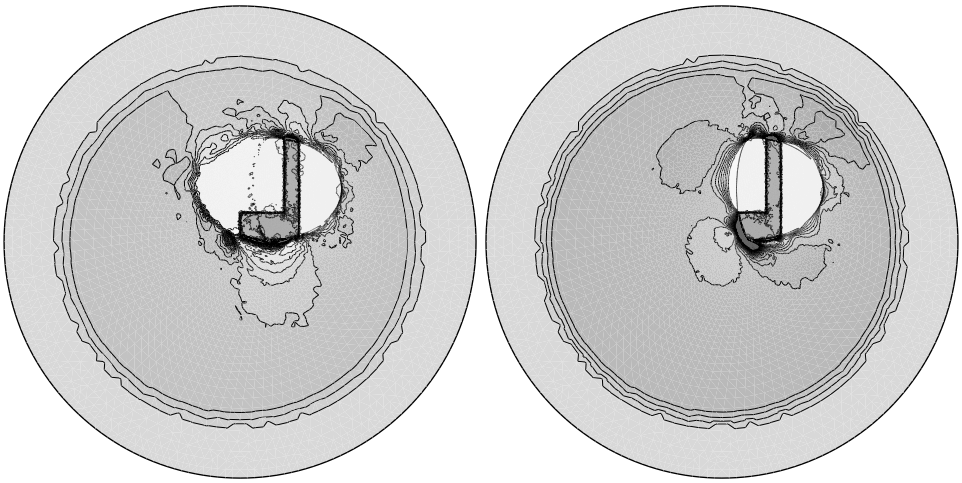

Figure 8. *The computed conductivity with the right patch only and then with both patches.*

patches, say ω_A, ω_B, and two different meshes adapted to each patch, we compute in parallel two objective functions,

$$\mathcal{J}_{1,\omega_A}(\sigma) := \int_{\omega_A} \left[\sqrt{E(\sigma)} - \sqrt{E(\sigma^\star)}\right]^2 dx,$$
$$\mathcal{J}_{1,\omega_B}(\sigma) := \int_{\omega_B} \left[\sqrt{E(\sigma)} - \sqrt{E(\sigma^\star)}\right]^2 dx,$$

each one being restricted to a given patch, on their own corresponding meshes (which are refined independently of each other) and the directions of descent they yield, namely, $d\sigma_A$ on the patch ω_A and $d\sigma_B$ on ω_B. The new objective function is defined as the average of these two objective functions, that is,

$$\mathcal{J}_1(\sigma) := \frac{1}{2}\left[\mathcal{J}_{1,\omega_A}(\sigma) + \mathcal{J}_{1,\omega_B}(\sigma)\right].$$

Then, the direction of descent on one mesh is the average of the computed direction of descent and the interpolation of the direction computed on the other mesh, that is, $(d\sigma_A + d\sigma_B)/2$. Each conductivity is then updated separately.

Figure 8 shows the resulting conductivities when the algorithm is applied with the right patch only and then when the algorithm takes the two patches into consideration in a parallel algorithm.

Figure 9 shows the convergence histories. We compare the convergence of the cost function $\mathcal{J}_1$ when the optimization is done on the complete ellipse with that of the patchwork approach. We see that the rate of convergence is comparable in all cases.

These convergence charts show that the parallel computation is as efficient as a global minimization algorithm. Note that, since the meshes are refined on both patches, the mesh precision of the parallel algorithm is almost twice that of the global minimization algorithm. This is the motivation of this parallelization approach: to obtain a finer precision in a reduced

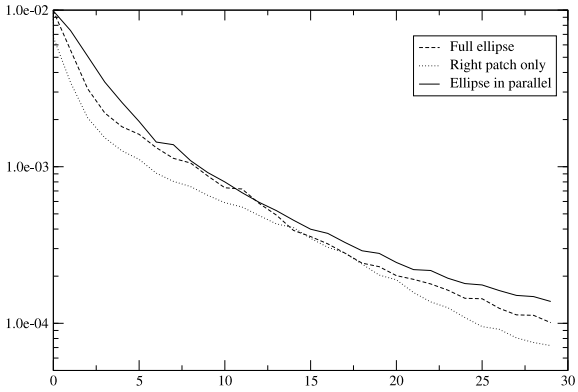

Figure 9. *The convergence of the cost function $\mathcal{J}_1$ for a subregion. The dashed line corresponds to the full ellipse reconstruction shown in Figure 6 (left). The dotted line corresponds to the optimization in the right patch only. The solid line corresponds to the two-patch parallel optimization.*

time. The parallel algorithm is not less efficient than the optimization on any of the two subregions. This shows that the error boundary layer which appears on the boundary of the patches is not a severe drift from the optimal solution, as it vanishes when the outside domain is updated. The parallelization of the algorithm is therefore relatively simple.

6. Numerical results using the cost function $\mathcal{J}_2$. In this section, the numerical results obtained for the cost function $\mathcal{J}_2$ are presented. Several boundary conditions $g_1, \dots, g_N$ are used to estimate the conductivity. The cost function is the sum of the cost functions associated to these boundary conditions: $\mathcal{J}_2 = \sum_{1 \le k \le N} \mathcal{J}_2^k$. The algorithms were implemented with piecewise linear finite elements, using `Getfem++` [10] and MATLAB. The results presented below were obtained with the combined algorithm introduced in section 4.2 (Algorithm 3).

6.1. Two-dimensional results: A half-disk. The domain $\Omega \subset \mathbb{R}^2$ is a half-disk of radius 1 centered at the origin; the conductivity σ is to be reconstructed in the half-disk ω of radius 0.9 centered at the origin. The value of the conductivity smoothly varies between 1 and 1.8 in the background, and a circular inclusion was added, with the radius of this inclusion 0.06 and the contrast of the conductivity 3. For the generation of the data, the domain Ω is meshed by 6004 triangles and 3088 vertices, and the mesh is adapted to the geometry of the inclusion.

There are $N = 2$ different boundary currents, equal to, respectively, x_1 and x_2 (the spatial coordinates), but for the bottom boundary of the domain that is considered as insulating (homogeneous Neumann condition). The local energy density is computed using piecewise affine finite elements. A Gaussian noise is added, with variance equal to 1% of the L^2-mean of the energy. The energy density is then interpolated on a finer mesh with 16064 triangles and 8193 vertices that is independent of the geometry of the inclusion. This fine mesh is used for the reconstruction.

The subdomain ω is meshed by 10400 elements. Hence there are 10400 unknowns, while the number of data is 10400 times the number of boundary currents applied. Algorithm 3 was used with the following parameters: six nested grid steps, followed by three Gauss–Newton steps. In Figure 10 the true conductivity (top left) and the estimated conductivity at several steps of Algorithm 3 are presented.

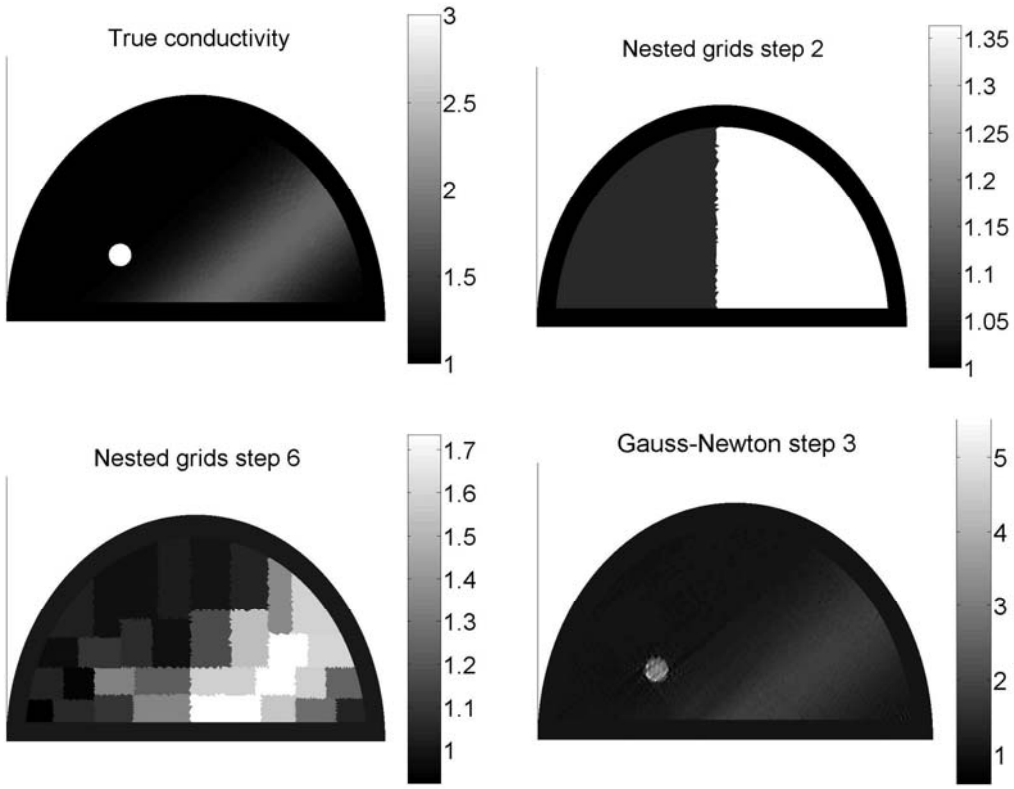

Figure 10. *Reconstruction process with* 1% *noise. Top left: the true conductivity to be recovered. Top right: nested grids algorithm after* 2 *steps, and then (bottom left) after* 6 *steps. Bottom right: the result after* 3 *steps of the Gauss–Newton algorithm applied to the bottom left result.*

6.2. Three-dimensional results: A half-sphere. A more realistic three-dimensional geometry was simulated in order to mimic breast examination. The domain Ω is a half-sphere of radius 1.1, the domain ω is a half-sphere of radius 0.9. The mesh of the domain ω contains 6321 convexes, the number of unknown conductivity coefficients. The numerical issues of interpolation between three-dimensional meshes were not addressed in this work, and the reconstruction is performed on the same mesh as the mesh that was used to generate the data.

The bottom of the half-sphere is insulating (homogeneous Neumann condition), and there are eight disk-shaped electrodes at the boundary; see Figure 11. One experiment consists of applying a Dirichlet condition to the electrodes, such that each electrode is at a given electric potential. The true conductivity $e^{\sigma^\star}$ is space-dependent, and there is a spherical inclusion of radius 0.1 with high conductivity and a background where the conductivity depends smoothly on the second space variable. The quantity $e^{\sigma^\star}|\nabla u^\star|^2$ is measured in ω.

There are $N = 4$ boundary conditions defined as follows: on each electrode a potential equal to, respectively, $g_1 = x_1$, $g_2 = x_2$, $g_3 = x_1 + x_2$, and $g_4 = x_1 - x_2$, where x_1 and x_2 are the first and second spatial coordinates of the center of mass of the electrode. We show g_1 and g_2 in Figure 12.

The nested grids algorithm described in section 4.2 was applied with the following pa-

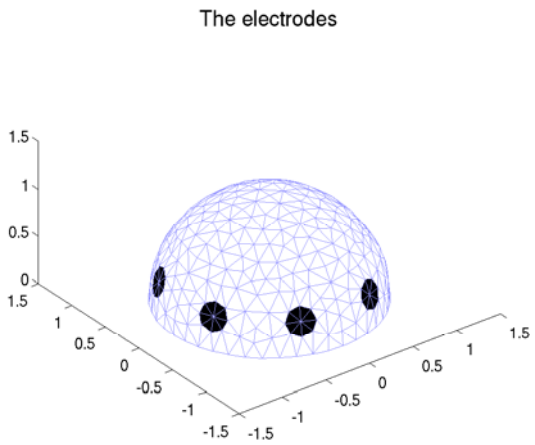

Figure 11. *Location of the electrodes (black circles).*

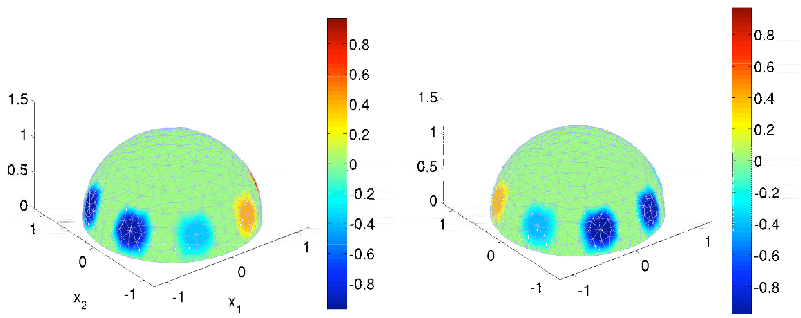

Figure 12. *The boundary conditions g_1 (left) and g_2 (right).*

rameters: two coarse nested grid steps and five fine Gauss–Newton steps. Figure 13 shows the logarithmic evolution of the discrepancy between the true conductivity and the reconstructed conductivity, as a function of the iterations (measured with different norms), with 0.01% and 2% Gaussian white noise. The complete resolution takes about 600s with a 1.73 GHz computer. Slice views of the reconstructed conductivity are shown in Figure 14.

Note. Other simulations were conducted with fewer boundary conditions ($N = 2$). In the absence of noise, the results of the reconstruction were analogous to the reconstruction with $N = 4$ different boundary conditions (but the speed is twice as fast, since the total number of conductivity problems to be solved is divided by a factor 2). However, in the presence of noise, taking into consideration four measurements allows us to reduce the variance of the noise (and hence the error in the retrieved conductivity). An application to real data should evaluate the number of experiments that provides the best trade-off between speed and noise variance reduction.

7. Conclusion. The first result of this paper is to show that in two dimensions, under sufficient local regularity assumptions, the local energy densities corresponding to two diffeomorphic boundary data uniquely determine the conductivity up to a multiplicative constant. We were not able, however, to prove such a result in three dimensions without prior infor-

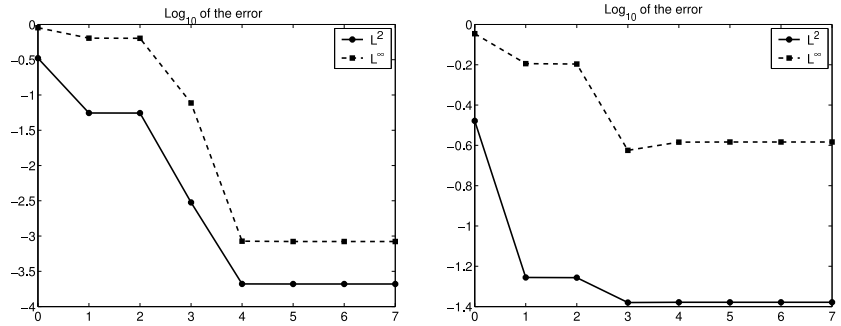

Figure 13. *Evolution of the* $\log_{10}$ *of the discrepancy between the true and the reconstructed conductivity:* 0.01% *noise (left) and* 2% *noise (right).*

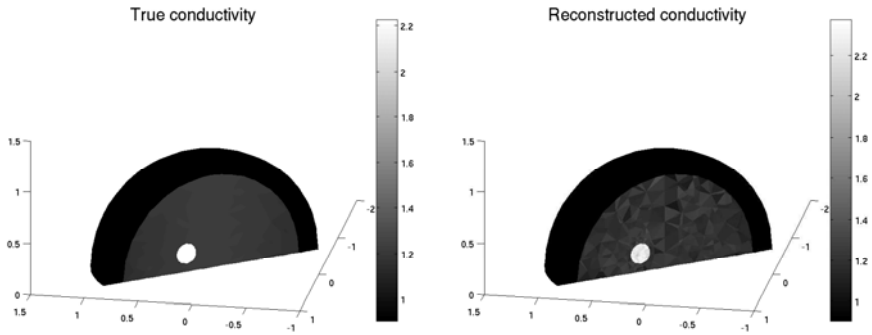

Figure 14. *Slice views of the true and the reconstructed conductivity with* 2% *noise.*

mation on the conductivity map. Sections 5 and 6 illustrate that despite these limitations, the conductivity can be successfully numerically reconstructed in two and three dimensions, even for irregular conductivity maps. We consider the reconstruction as a minimization problem and apply classical optimization techniques. Although the Hessian of the functional we minimize fails to be strictly convex, choosing at each time step either a positive or a negative increment allows us to overcome that problem. We do not address the question of the theoretical well-posedness of the minimization problem. Instead, we investigate it numerically. Due to computational power limitations, our numerical calculations in three dimensions are not exempt from some "inverse crime"; namely, the same mesh is used for the creation of the synthetic data and for the reconstruction. However, we did consider the case of noisy data. In two dimensions, however, we do not have such a limitation, and several computations are performed on independent meshes.

Our computations indicate that the problem is not very ill-posed in practice. The dependence on the boundary geometry is not severe, and in the presence of 10% of white noise, the error in the reconstructed conductivity map stays within approximately 10% of the target. This is a striking difference from the usual electrical impedance tomography problem, which is known to be very severely ill-conditioned (see, e.g., [3]), and where numerical experiments such as the ones we conducted would have been fatal to the reconstruction. In particular, we do not need to rely on any Tikhonov regularization, in contrast to what is done in [5] when only the Dirichlet-to-Neumann map is available.

Acknowledgment. This paper has been improved significantly by the suggestions of the referees, and we would like to thank them.

REFERENCES

[1] G. Alessandrini and V. Nesi, *Univalent σ-harmonic mappings*, Arch. Ration. Mech. Anal., 158 (2001), pp. 155–171.
[2] H. Ammari, E. Bonnetier, Y. Capdeboscq, M. Tanter, and M. Fink, *Electrical impedance tomography by elastic deformation*, SIAM J. Appl. Math., 68 (2008), pp. 1557–1573.
[3] L. Borcea, *Electrical impedance tomography*, Inverse Problems, 18 (2002), R99–R136.
[4] M. Briane, G. W. Milton, and V. Nesi, *Change of sign of the corrector's determinant for homogenization in three-dimensional conductivity*, Arch. Ration. Mech. Anal., 173 (2004), pp. 133–150.
[5] D. C. Dobson, *Convergence of a reconstruction method for the inverse conductivity problem*, SIAM J. Appl. Math., 52 (1992), pp. 442–458.
[6] D. Gilbarg and N. S. Trudinger, *Elliptic Partial Differential Equations of Second Order*, Springer-Verlag, Berlin, 1983.
[7] W. Hackbusch, *Multigrid Methods and Applications*, Springer Ser. Comput. Math. 4, Springer-Verlag, Berlin, 1985.
[8] F. Hecht, O. Pironneau, A. Le Hyaric, and K. Ohtsuka, *FreeFem++* Version 2.20, Laboratoire Jacques-Louis Lions, UMR 7598, Université Pierre et Marie Curie, Paris, 2007.
[9] R. S. Laugesen, *Injectivity can fail for higher-dimensional harmonic extensions*, Complex Var. Theory Appl., 28 (1996), pp. 357–369.
[10] Y. Renard and J. Pommier, *Getfem++, a Generic Finite Element Library in C++*, Laboratoire MIP, UMR 5640, Université Paul Sabatier, Toulouse, France, 2007.